

The structure and variability of Mars dayside thermosphere from MAVEN NGIMS and IUVS measurements: Seasonal and solar activity trends in scale heights and temperatures

Stephen W. Bougher¹, Kali Roeten¹, Kirk Olsen¹, Paul R. Mahaffy², Mehdi Benna^{2,3}, Meredith Elrod^{2,4}, Sonal Jain⁵, Nicholas M. Schneider⁵, Justin Deighan⁵, Ed Thiemann⁵, Francis G. Eparvier⁵, Arnaud Stiepen⁶, and Bruce Jakosky⁵

S. W. Bougher bougher@umich.edu

¹Climate and Space Sciences and Engineering Department, University of Michigan, Ann Arbor, Michigan, USA.

²Planetary Environments Laboratory, Code 699, NASA Goddard Space Flight Center, Greenbelt, Maryland, USA.

³CRESST, University of Maryland, Baltimore County, Baltimore, Maryland, USA.

This article has been accepted for publication and undergone full peer review but has not been through the copyediting, typesetting, pagination and proofreading process, which may lead to differences between this version and the Version of Record. Please cite this article as doi: 10.1002/2016JA023454

Abstract.

Mars dayside thermospheric temperature and scale height trends were examined using measurements from the Neutral Gas Ion Mass Spectrometer (NGIMS) and the Imaging Ultraviolet Spectrograph (IUVS) on the Mars Atmosphere Volatile Evolution (MAVEN) spacecraft. Average scale heights (over 150-180 km for solar zenith angles $\leq 75^\circ$) from several different sampling periods were obtained from each instrument. NGIMS and IUVS scale height trends were found to be in good agreement, with both showing scale heights decreasing after perihelion and reaching a low value near aphelion (13.6 to 9.4 km). Between these two seasonal extremes, the temperature decreased by ~ 70 K (from 240 to 170 K). These trends were also analyzed with respect to the changing solar flux reaching the planet, using the Lyman-alpha irra-

⁴CRESST, University of Maryland,
College Park, Maryland, USA.

⁵Laboratory for Atmospheric and Space
Physics, University of Colorado Boulder,
Boulder, Colorado, USA.

⁶Laboratoire de Physique Atmosphérique
et Planétaire, Space Sciences, Technologies
and Astrophysics Research (STAR)
Institute, University of Liège, Belgium.

diance measured by the Extreme Ultraviolet monitor (EUVM) on MAVEN.

Scale heights responded strongly to the changing solar flux. During this part of the MAVEN mission (October 2014 to May 2016), it was concluded that over longer time scales (at least several months), dayside thermospheric temperatures are chiefly driven by changing solar forcing, although it is the effects of changing heliocentric distance rather than changing solar activity which seem to have the greatest impact. Furthermore, effects of solar forcing were not observed on shorter time scales (less than a month), suggesting local wave effects may dominate solar forcing on these time scales. Finally, temperatures from two NGIMS sampling periods were compared to temperatures from the Mars Global Ionosphere-Thermosphere Model (M-GITM) and found to be in good agreement.

Keypoints:

- Seasonal and solar activity trends of Mars dayside upper atmosphere are revealed by MAVEN
- MAVEN NGIMS and IUVS dayside thermosphere scale height trends are very similar
- Long-term variability of Mars dayside thermospheric temperatures is tied to solar driven thermal balances

1. Introduction and Motivation

A thorough characterization of the mean structure and variability of the Martian day-side thermosphere (i.e. temperatures, densities, winds, and waves over ~ 100 -250 km) is important for understanding its temporal responses to external forcing. It is notable that the Martian thermosphere is an intermediate atmospheric region strongly coupled to the lower-middle atmosphere below (e.g. seasonal inflation/contraction, gravity waves, planetary waves, thermal tides, dust storms) and also coupled above with energy inputs from the Sun (soft X-ray, EUV, and UV fluxes, and solar wind particles) (see reviews by *Bougher et al.* [2015a]). At present, the relative roles of solar forcing and wave forcing (at different times in the solar cycle and throughout the Martian year), and their ability to maintain the observed structure and drive the variability of the upper atmosphere, have yet to be fully quantified. Such a systematic characterization will provide constraints for the changing thermal budget of the dayside thermosphere, which serves to regulate the temporal responses (i.e. solar cycle, solar rotational, seasonal, and diurnal responses) of the upper atmosphere.

The nominal thermal balance in the Mars dayside upper thermosphere is estimated to occur between solar EUV heating and cooling by molecular thermal conduction, while below 130 km, CO₂ 15- μ m cooling plays a larger role (see reviews by *Bougher et al.* [1999, 2015a]). Furthermore, the amount of solar EUV radiation largely responsible for heating the Martian thermosphere undergoes significant variation over time, and must be measured locally at Mars to clearly link solar forcing and thermal responses [e.g. *Eparvier et al.*, 2015; *Bougher et al.*, 2015a]. This substantial variability is due to the

large eccentricity of Mars orbit (1.38-1.67 AU), the obliquity producing the seasons, and variations in solar output to which both the 27-day solar rotation and 11 year solar cycle contribute [e.g. *Woods and Rottman*, 2002; *Bougher et al.*, 2015a]. For instance, the 27-day solar rotation often gives rise to a modulation of the solar EUV and UV fluxes received at the planet, which may be reflected in corresponding temperature variations of the Mars dayside thermosphere. Furthermore, changing heliocentric distance and the seasonal cycle in particular are usually considered together due to the proximity of the solstices to perihelion and aphelion and the resulting difficulty in separating their effects. [e.g. *Bougher et al.*, 2015a]. Overall, this variability in the EUV fluxes received at Mars has been predicted to produce significant variations in composition, temperature, and winds in the thermosphere [e.g. *Bougher et al.*, 2002, 2015b; *Forbes et al.*, 2008; *González-Galindo et al.*, 2009].

Nevertheless, wave forcing of the upper atmosphere densities, temperatures, and wind structure may also be important and is beginning to be examined with tidal and gravity wave modeling. Gravity wave momentum and energy deposition, owing to the breaking of upward propagating waves, may produce changes in the mean wind structure as well as the temperatures of the upper atmosphere [*Medvedev et al.*, 2011; *Medvedev and Yigit*, 2012; *Medvedev et al.*, 2013]. Evidence of these impacts is apparent in the winter polar warming signatures first observed in aerobraking datasets [*Keating et al.*, 2003, 2008; *Bougher et al.*, 2006]. This implies that a full description of the upper atmosphere structure and dynamics may require a combination of both solar forcing and wave forcing mechanisms [e.g. *Medvedev et al.*, 2015].

The MAVEN mission is beginning to collect in-situ and remote datasets throughout the Martian seasons and at various solar activity levels, allowing for a more systematic characterization of the upper atmosphere. In addition, solar EUV-UV flux measurements are now available from MAVEN to monitor the solar irradiance at Mars for the first time. In this paper, we focus upon a detailed examination of the dayside thermal structure and its seasonal and solar activity trends (and corresponding solar drivers) as observed by newly obtained MAVEN spacecraft datasets.

1.1. Brief review of pre-MAVEN dayside upper atmosphere temperatures

Prior to MAVEN (the Mars Atmosphere and Volatile Evolution Mission), the Martian upper atmosphere thermal structure (both dayside and nightside) was poorly constrained by a limited number of both in-situ and remote sensing measurements at diverse locations, seasons, and periods scattered throughout the solar cycle (see reviews by *Stewart* [1987]; *Bougher et al.* [2000]; *Mueller-Wodarg et al.* [2008]; *Bougher et al.* [2015a]). The vertical thermal structure of the upper atmosphere has been sampled many times, but only in specific latitude and local time zones and mostly during solar minimum to moderate conditions [*Bougher et al.*, 2015b]. These limited dayside temperature measurements included in-situ sampling from: (a) Viking Landers 1 and 2 entry accelerometers (based on mass density scale heights) [*Seiff and Kirk*, 1977], (b) Viking Landers 1 and 2 Upper Atmosphere Mass Spectrometers (UAMS) (based on neutral density scale heights) [*Nier and McElroy*, 1977], (c) the Mars Global Surveyor (MGS) Accelerometer Experiment [e.g. *Keating et al.*, 1998, 2003, 2008; *Bougher et al.*, 2015a], and (d) the MGS application of the precise orbit determination technique (which was used to derived densities and scale heights from 1999 to 2005) [*Forbes et al.*, 2008]. Recently, observations from Mars

Express MARSIS (Mars Advanced RADAR for Subsurface and Ionospheric Studies) were used to find the equivalent slab thickness of the ionosphere from which thermospheric temperatures were derived [Mendillo *et al.*, 2015]. In addition, remote measurements of key dayglow emissions (e.g. CO Cameron bands and CO₂⁺ ultraviolet doublet (UVD)) were obtained by Mariners 4, 6, 7, 9, and Mars Express and have been used to extract dayside thermospheric temperatures [e.g. Stewart, 1972; Stewart *et al.*, 1972; Leblanc *et al.*, 2006; Huestis *et al.*, 2010; Stiepen *et al.*, 2015]. A brief summary of selected pre-MAVEN dayside topside thermospheric temperatures (for solar minimum to moderate conditions) is presented in Table 1.

The significant Mars orbit eccentricity (i.e. changing heliocentric distance) demands that both the solar cycle and seasonal variations be considered together when examining temperature trends in the dayside thermosphere and exosphere [e.g. Bougher *et al.*, 2000, 2015a]. These combined variations are difficult to quantify without systematic measurements. As a result, considerable debate and study have resulted regarding the Martian dayside temperature structure and its variability since the first Mariner ultraviolet spectrometer (UVS) measurements were made (1969 -1972) [e.g. Stewart, 1972; Stewart *et al.*, 1972; Stewart, 1987]. Prior to MAVEN, the collection of limited in-situ and remote temperature measurements together enabled a rough composite estimate to be made of the extreme solar cycle plus seasonal variations of Martian dayside exospheric temperatures, from ~180-200 K to ~350 K (see Forbes *et al.* [2008]; Bougher *et al.* [2015a]). This estimate is most uncertain for solar moderate-to-maximum conditions, for which little data is available.

Finally, the most recent pre-MAVEN study of upper atmosphere dayside temperature variations focused on 10 years of Mars Express SPICAM (Spectroscopy for Investigation of Characteristics of the Atmosphere of Mars) ultraviolet dayglow emission measurements [Stiepen *et al.*, 2015]. Mean temperatures were extracted over 150-180 km, based upon CO Cameron and CO₂⁺ dayglow profiles fit with an exponential function. Scale heights were found to be highly variable, ranging from 8.4 to 21.8 km (corresponding to ~153 to 400 K). Stiepen *et al.* [2015] observed no correlation between solar zenith angle (SZA) and temperatures across the dayside, consistent with previous studies of Leblanc *et al.* [2006]. In addition, solar activity, as determined by the F10.7-cm index rotated to Mars (i.e. corrected for the Sun-Earth-Mars angle), did not appear to influence scale height (or temperature) variability over the 10-year observing period (spanning solar minimum to moderate conditions), again consistent with smaller dataset studies [Leblanc *et al.*, 2006]. This latter finding would imply that large local variations in scale heights dominate over the long-term control exerted by solar forcing. They posited that these large local variations may be driven by upward propagating gravity waves and tides, which served to overwhelm the solar forcing control during this sampling period and provide heating. However, lower atmosphere impacts upon upper atmosphere temperature structure have yet to be fully characterized.

1.2. Motivation for comparing new MAVEN NGIMS and IUVS datasets

Jain *et al.* [2015] reported a first study of MAVEN IUVS dayglow observations focused upon upper atmosphere structure and variability. Similar to Stiepen *et al.* [2015], the 150 to 180 km region of the dayside thermosphere was selected to derive scale heights (and corresponding temperatures) from CO Cameron band and CO₂⁺ UVD emission profiles

assuming an isothermal atmosphere. Two sampling periods were utilized (Ls = 218: 18-22 October 2014; Ls = 337-352: 5 May 2015 to 2 June 2015), each exhibiting SZAs less than about 73 degrees. However, a major advance for this study was simultaneous monitoring of both the UV dayglow and the local EUV flux received at Mars. This enables the longer-term solar forcing signal to be distinguished from the short-term local variability of the thermosphere. Specifically, the mean scale height for the two seasons was found to be 16.2 ± 0.1 km and 14.0 ± 0.1 km, with a standard deviation of 1.6 km for both (owing to the intrinsic variability of the thermosphere). These scale heights correspond to mean temperatures of 300.0 ± 2.0 K and 250.6 ± 1.7 K, respectively, with a common standard deviation of ~ 29 K. These two measurements reveal a ~ 50 K cooling over this time period between October 2014 and May 2015, consistent with the decrease in solar activity and the increase in heliocentric distance between these two seasons. This indicates that the influence of solar forcing upon thermospheric temperatures is dominant on the longer time scales represented by these two seasons. Additional sampling periods distributed over Mars seasons and different levels of solar activity are needed to further characterize the longer term seasonal and solar cycle trends of dayside thermospheric temperatures at low SZAs.

Of equal importance is the lack of correlation of solar EUV fluxes (17-22 nm channel) from the MAVEN Extreme Ultraviolet monitor (EUVM) instrument and temperatures on a selected shorter time scale (5-18 May 2015). This implies that on short time scales (when solar flux variations are small), the temperature variability in the thermosphere depends less on solar forcing and more on wave and/or tidal activity from the lower atmosphere [Jain *et al.*, 2015]. This result is consistent with the previous studies of Stewart [1972]

and *Leblanc et al.* [2006] which found a lack of correlation of temperature variations and solar EUV fluxes on short time scales, and *Leblanc et al.* [2006] and *Stiepen et al.* [2015] on longer time scales.

A much larger IUVS dayglow dataset of CO Cameron band and CO₂⁺ UVD emissions can now be utilized to address the long and short term trends of solar EUV fluxes and dayside thermospheric scale heights and temperatures (see *Jain* [2016]). In addition, a large dataset of NGIMS neutral density profiles can also be used to extract 150-180 km mean temperatures from thermospheric regions that match closely to the low SZA sampling periods and altitude region chosen in the IUVS studies. Such a dedicated instrument inter-comparison study is crucial to the confirmation and further extension of the longer term (solar driven) and shorter term (wave driven) trends in dayside temperatures first identified in the *Jain et al.* [2015] paper.

1.3. Motivation for comparing these MAVEN datasets with M-GITM

The seasonal and solar cycle trends in extracted 150-180 km mean dayside temperatures that are sought in this new cross-instrument comparison study will also benefit from comparison with solar driven global models. Specifically, the Mars Global Ionosphere-Thermosphere Model (M-GITM) is primarily solar driven and is designed to capture the major processes that regulate the thermospheric energetics and dynamics on longer time scales [*Bougher et al.*, 2015b]. It is anticipated that the comparison of extracted M-GITM temperatures (along the MAVEN orbit trajectories) and IUVS and NGIMS derived temperatures will provide insight into the underlying thermal balances responsible for these measured long term variations. Data-model discrepancies will point to missing

physical processes that can be incorporated into the model to better capture the measured temperature trends.

An overview of this paper is as follows. Section 2 will describe the MAVEN datasets and the corresponding sampling periods used in this study. Section 3 reviews the salient features, capabilities, and intended applications of the M-GITM framework and its outputs for use in the data-model comparisons. Results are presented and their implications are discussed in section 4. And finally, section 5 summarizes key conclusions and the next steps as this research goes forward.

2. MAVEN Datasets used

Densities are obtained from NGIMS measurements and derived from IUVS dayglow observations, from which scale heights can be calculated. These datasets can be used in tandem to characterize thermospheric scale height and temperature trends across the dayside of Mars. Several periods of orbits during different Martian seasons throughout the MAVEN mission were analyzed, ranging from October 2014 to May 2016, in order to examine the Martian thermosphere over time.

To make the comparison between NGIMS and IUVS derived scale heights as close as possible (i.e. compatible with nearly the same volume of atmosphere, and subject to nearly the same solar, seasonal and location conditions), orbits were chosen for the analysis which met the same initial set of criteria: (1) orbits had data within the altitude range of 150-180 km and (2) orbits had SZAs less than 75° within that altitude range.

Relatively low SZAs, less than 75° , were selected in order to ensure the data from IUVS would be from the dayside. This was necessary as IUVS dayglow emission measurements were used to derive scale heights. Furthermore, studies from both IUVS and NGIMS have

indicated that at thermospheric altitudes, temperature, and by extension, scale height, does not vary significantly with relatively low SZA. *Mahaffy et al.* [2015a] showed that over a significant part of the Martian year, from northern hemisphere winter solstice to near equinox, for solar zenith angles below 75° at 200-300 km, temperature shows no clear variation with SZA. A similar lack of correlation was seen between IUVS derived scale heights and solar zenith angles over the thermospheric altitude range of 150-180 km [*Jain et al.*, 2015]. Thus, different relatively low SZAs should not contribute notably to thermospheric scale height trends.

In addition to the SZA criterion, only the segment of the orbits within the upper thermospheric altitude range of 150-180 km was considered. This is the same altitude range that was applied by the *Jain et al.* [2015] and *Stiepen et al.* [2015] analyses of scale heights derived from dayglow emissions. Below 180 km where fluorescent scattering is not a significant process, it has been found that the scale height of the CO_2^+ UVD emission is directly linked to the neutral CO_2 atmospheric scale height [e.g. *Stiepen et al.*, 2015]. Furthermore, thermospheric scale heights can be derived from the IUVS measurements of CO_2^+ and CO Cameron emissions assuming the thermosphere is nearly isothermal [*Stewart et al.*, 1972]. The lower boundary of 150 km was chosen as it often occurs near the altitude where temperatures in the upper atmosphere no longer undergo significant change with height [e.g. *Bougher et al.*, 2015a; *Stiepen et al.*, 2015], although this altitude is believed to vary in response to the changing solar fluxes received at the planet [*Bougher et al.*, 1999, 2015b].

It should be noted that although applying these criteria to both IUVS and NGIMS datasets allows for a closer comparison of thermospheric scale heights, there are still

unavoidable differences, especially due to instrument sampling. Since NGIMS takes measurements along the spacecraft's track and IUVS is a remote sensing instrument, for any particular orbit, they will not necessarily be measuring the same volume of atmosphere [Jakosky *et al.*, 2015]. As a result, the orbits which meet the two criteria are different for each instrument. This also results in different numbers of orbits in each sampling period for both IUVS and NGIMS. The combination of these factors makes a direct comparison between scale heights derived from the two instruments difficult. However, since average scale heights spanning multiple orbits are used in this analysis, some of the local variations due to the different observing geometry are eliminated. Furthermore, trends in scale height can still be compared. This will primarily be the focus for comparison between the NGIMS and IUVS scale heights in this paper.

2.1. NGIMS datasets and sampling periods used

The Neutral Gas Ion Mass Spectrometer (NGIMS) is a quadrupole mass spectrometer on the MAVEN spacecraft designed to measure the composition of the major neutral gas and ion species in the upper atmosphere with a vertical resolution of ~ 5 km and a target accuracy of $<25\%$ for most species. Measurements are taken along the spacecraft track typically over the 150 to 500 km altitude region. NGIMS alternates between a closed source mode, which measures non-reactive neutral species (e.g. CO_2 , Ar, N_2 , He), and an open source mode which measures both surface reactive neutral species (e.g. O, CO, NO) and ambient ions [Mahaffy *et al.*, 2015b].

The NGIMS dataset used for this analysis is the Level 2, Version 6, Revision 2 (V06_R02) product. This dataset gives single species abundances which have been converted from detector count rates and corrected for instrument background [Mahaffy *et al.*, 2015b].

While this is the most recent data release available, there are still further corrections planned to take place during the next release, including a reduction of CO₂ densities following the first Deep Dip campaign (a week-long lowering of periapsis to ~125 km [Jakosky *et al.*, 2015; Zurek *et al.*, 2015]) by a factor of about 1.5 to account for detector gain changes. Since this correction does not vary with height, it should not alter the derived temperature profiles from that time period since only the absolute density will be adjusted.

Seven sampling periods were identified in the 15-month NGIMS dataset which met both the SZA and the altitude range criteria. More detailed information about these orbit periods is given in Table 2. These periods range from March 2015 to May 2016, over one year of the MAVEN mission. This corresponds to about 60% of a Martian year, with solar longitudes from $L_s = 306$ to $L_s = 156$. During this time, the season changed from near perihelion to near northern hemisphere autumnal equinox. The local time, latitude, and SZA range for each period are provided in Table 2.

One factor unique to NGIMS that significantly limited the orbits which could be selected for the analysis was the altitude range. Although MAVEN's nominal periapsis altitude during science orbits is 150 km, the spacecraft does not always reach this altitude since a density corridor is targeted at periapsis rather than an altitude corridor [Jakosky *et al.*, 2015; Zurek *et al.*, 2015]. As a result, only a few periods of NGIMS orbits strictly met both the altitude and the SZA criteria. Thus, for several of the NGIMS orbit periods, a minimum altitude between 150 km and 160 km was permitted. These minimum altitudes are also supplied in Table 2.

Temperatures were extracted from the NGIMS dataset by vertically integrating densities from the top down to obtain pressures. Assuming that the vertical density profile is in hydrostatic equilibrium, the hydrostatic equation is integrated for CO₂ to obtain the local partial pressure. The temperature can then be calculated from the pressure using the ideal gas law and the CO₂ density measured by NGIMS. Various upper boundary conditions (pressures) were tested and their impact on the topside temperature profile examined. The altitude was then identified below which the temperature profile was close to identical for all choices of the upper boundary condition. This altitude was somewhat higher for perihelion (200-220 km) versus aphelion (190-200 km) sampling periods, thus determining the altitude range of our extracted temperatures. This same basic method of deriving temperature profiles from densities was recently used in *Snowden et al.* [2013], and is described in greater detail there. Temperatures in this study were calculated from CO₂ and Ar densities, as seen in the temperature profiles in Figure 2. Scale heights were then calculated from the CO₂ temperature profile using the definition of scale height derived from the equation of hydrostatic balance and the ideal gas law. Only data from the inbound leg of the orbit was used due to calibration difficulties with the background subtraction of accumulated CO₂ densities on the outbound leg [e.g. *Mahaffy et al.*, 2015b]. For each inbound segment of the orbit, scale height and temperature profiles were derived and restricted to the 150-180 km altitude range. Averaging was then done over each period of orbits to create average profiles and remove most of the high frequency variability of any individual orbit which could mask longer time scale trends. These profiles were then averaged over the 150-180 km altitude range to find a representative scale height and temperature for each sampling period.

2.2. IUVS datasets and sampling periods used

The Imaging Ultraviolet Spectrograph (IUVS) is a ultraviolet remote sensing instrument onboard the MAVEN spacecraft. It has two detectors: a far ultraviolet (FUV) detector (115-190 nm) and a mid ultraviolet (MUV) detector (180-340 nm), with a spectral resolution of 0.6 and 1.2 nm, respectively. IUVS is mounted on an Articulated Payload Platform (APP) that allows controlled orientation of IUVS's field of view relative to Mars and provides desired viewing geometry. IUVS limb measurements are taken near periapse with slit ($11.3^\circ \times 0.06^\circ$) pointed perpendicular to the spacecraft motion [McClintock *et al.*, 2014]. IUVS uses a scan mirror to sweep the slit up and down to map the vertical profile of the atmosphere with an altitude resolution of ~ 5 km. In a single orbit IUVS takes 12 limb scans [see Jain *et al.*, 2015; Jain, 2016, for more detail]. The observed raw data numbers (DN) are corrected for detector dark current and then converted to physical brightness in Rayleigh using the sensitivity derived from UV bright stellar observations made during the MAVEN cruise phase [McClintock *et al.*, 2014]. The MUV and FUV systematic uncertainties estimated from these stellar calibrations are $\pm 30\%$ and $\pm 25\%$, respectively. The flatfield errors have not been corrected in the data, which can introduce additional 10% uncertainty. The data used in this analysis can be downloaded from the atmosphere node of NASA's Planetary Data System. The data files are tagged "periapse" with version/revision tag V06_R01.

In the present analysis we selected time periods of IUVS dayglow observations based on their overlap with NGIMS data. Table 3 shows the lighting and geometry for IUVS observations used in this analysis.

We have used an empirical Chapman fit to CO₂⁺ ultraviolet doublet (at 290 nm) emission intensity to determine scale heights. This method is similar to what has been used by *Lo et al.* [2015] on CO₂⁺ intensity observed by IUVS to study the non-migrating tides.

We used an integral of parameterized volume emission rate (see Equation 1) to fit the measured intensity using the Levenberg-Marquardt least squares minimization algorithm:

$$I = 2 \int_b^\infty \Pi_F \sigma n_0 \exp\left(\frac{z_0 - z}{H} - \frac{\sigma n_0 H}{\cos(\chi)} e^{(z_0 - z)/H}\right) \frac{r dz}{\sqrt{r^2 - b^2}} \quad (1)$$

where Π_F accounts for solar flux and calibration factors; z is the altitude; b is the tangent altitude of the line of sight from the center of the planet; z_0 is the reference altitude, which is set at 130 km in this analysis; H is the scale height; $r = R + z$, where R is the radius of Mars; χ is the solar zenith angle; σ_0 is the photo-absorption cross section of UV photon; and n_0 represents density of CO₂ at the reference altitude of z_0 . The three parameters, viz., Π_F , H , and scaled density $\sigma_0 n_0$ are allowed to vary during the fit. Figure 1 shows an example of the Chapman fit to the observed intensity of CO₂⁺ UVD emission.

2.3. EUV dataset used

Data from the Extreme Ultraviolet monitor (EUVM) on MAVEN was also used to examine the role of EUV flux as a possible driver of dayside thermospheric temperatures in this study. The EUV monitor is one of two quasi-independent components of the Langmuir Probe and Waves (LPW) instrument, the other being the LPW component [*Jakosky et al.*, 2015; *Eparvier et al.*, 2015]. The EUV monitor measures the variable solar soft x-ray, EUV, and UV irradiance received at Mars with three broadband filter radiometers. These radiometers measure the wavelength bands of 0.1-7 nm, 17-22 nm, and 121-122 nm (Lyman-alpha) emission, respectively. The EUVM dataset used in this

analysis is the Level 2, Version 5, Revision 4 (V05_R04) product, which gives the calibrated solar irradiance (W/m^2) for the three bands at a one second cadence. The Lyman-alpha irradiance, which is specifically used in this study as an indicator of the changing EUV-UV heating in the thermosphere, is given as a daily mean value [Eparvier *et al.*, 2015]. This dataset extends from October 2014 to June 2016, allowing for an analysis of solar output at this wavelength band concurrent with NGIMS and IUVS measurements.

3. M-GITM formulation and its application to dayside temperature trends

The Mars Global Ionosphere-Thermosphere Model (M-GITM) is a model framework combining the terrestrial GITM framework [Ridley *et al.*, 2006] with Mars fundamental physical parameters, ion-neutral chemistry, and key radiative processes in order to capture the basic observed features of the thermal, compositional, and dynamical structure of the Mars atmosphere from the ground to ~ 250 km [Bougher *et al.*, 2015b]. The GITM framework relaxes the assumption of hydrostatic equilibrium, and explicitly solves for vertical velocities that can potentially be large under extreme conditions (e.g. in areas of strong localized heating that may result from solar energetic particle events as well as extreme solar wind conditions). However, the current Mars upper atmosphere and the simulated M-GITM atmosphere are typically in hydrostatic balance (i.e. characterized by small vertical velocities) for normal driving conditions [Bougher *et al.*, 2015b]. The ongoing objectives for this M-GITM code include: (a) investigating the thermal and dynamical coupling of the Mars lower and upper atmospheres, (b) providing an accurate representation of the observed thermosphere-ionosphere structure and its variations over the Mars seasons and solar cycle, and (c) linking M-GITM (thermosphere-ionosphere structure) with other exosphere and plasma models in order to address Mars atmospheric

escape processes and determine modern escape rates [Bougher *et al.*, 2015a, b]. These objectives also support the MAVEN mission.

M-GITM simulates the conditions of the Martian atmosphere all the way to the surface.

For the Mars lower atmosphere (0-80 km), a correlated-k radiation code was adapted from the NASA Ames MGCM [Haberle *et al.*, 2003] for incorporation into M-GITM. This provides solar heating (long and short wavelength), seasonally variable aerosol heating, and CO₂ 15- μ m cooling in the LTE region of the Mars atmosphere (below \sim 80 km). For the Mars upper atmosphere (\sim 80 to 250 km), a fast formulation for NLTE CO₂ 15- μ m cooling was implemented into the M-GITM code [López-Valverde *et al.*, 1998; Bougher *et al.*, 2006] along with a correction for NLTE near-IR heating rates (\sim 80-120 km). In addition, a comprehensive set of cross sections and yields has been supplied for a CO₂ atmosphere, yielding the calculation of in-situ solar heating (EUV-UV), dissociation, and ionization rates at each model time step. Finally, a comprehensive set of 30+ key ion-neutral chemistry reactions and rates has been incorporated into the M-GITM code [e.g. Fox and Sung, 2001]. At this point, M-GITM assumes photochemical equilibrium when solving for the ionosphere (above \sim 80 km). Recently, Mars crustal fields have been added to the M-GITM framework, which will be important when ion transport effects (above \sim 200 km) are addressed in the future.

Simulated three-dimensional upper atmosphere fields include neutral temperatures, densities (CO₂, CO, O, N₂, O₂, He, etc), winds (zonal, meridional, vertical), and photochemical ions (O⁺, O₂⁺, CO₂⁺, N₂⁺, and NO⁺). Future minor species will include N(⁴S) and N(²D). Simulations spanning the full range of applications of the current M-GITM code,

including 12 model runs spanning various solar cycle and seasonal conditions, have been completed and the results are described in an archival paper [Bougher *et al.*, 2015b].

It is notable that M-GITM upper atmosphere physics, chemistry, and formulations are the most complete, and therefore data-model comparisons thus far have largely focused on this region above ~ 100 km. To date, M-GITM simulations have been compared with MAVEN NGIMS measurements obtained during its first year of operations during four Deep Dip campaigns [e.g. Bougher *et al.*, 2015c, d]. In particular, Deep Dip 2 (DD2) temperatures and key neutral densities have been compared with corresponding M-GITM fields extracted along DD2 orbit trajectories on the dayside near the equator [Bougher *et al.*, 2015c]. These comparisons reveal that M-GITM neutral temperatures match DD2 campaign averaged measurements very well at low SZAs, both approaching ~ 260 - 270 K at/above 200 km.

4. Results and Implications

4.1. NGIMS averaged temperature trends spanning all sampling periods

The average temperature profiles produced for each of the seven sampling periods plotted with 1-sigma orbit-to-orbit variability can be seen in Figure 2. For comparison, average temperatures were derived from both Ar and CO₂ densities. Argon measurements are currently the best calibrated due to the inert nature of the species. Comparing the CO₂ derived temperatures to those of Ar shows that on average (for the 150-180 km altitude range) the greatest difference is only 7.7 K and occurs during orbits 2194-2274. As can be seen in the profiles, there is often a larger difference between these derived temperatures at higher altitudes, such as in the profiles from orbits 1900-2000. This temperature difference is due to an instrument effect. During the inbound segment of the orbit, the sensors inter-

nal metal surfaces tend to adsorb atmospheric gases (i.e. CO₂ is better adsorbed than Ar), which artificially reduces the density measured by the instrument. Gas-wall interaction is not unique to the NGIMS sensor and has been observed and reported for other similar atmospheric investigations [*Cui et al.*, 2009; *Teolis et al.*, 2010]. Since the efficiency of gas adsorption rapidly diminishes as the sensors walls reach saturation, the altitude profile of the measured density will exhibit a steeper slope than it should have (and thus a lower apparent temperature). It is expected that the CO₂ derived temperature will always be cooler than that of Ar at higher altitudes, and the two gas temperatures should merge at low altitude (i.e. where the sensor's faces are fully saturated and adsorption ceases to be important). That is indeed what Figure 2 profiles illustrate. Nevertheless, while this difference between Ar and CO₂ derived temperatures exists, it is sufficiently small over the 150-180 km altitude range for our study. Thus, CO₂ derived temperatures and scale heights were examined to better correspond to the IUVS values which are derived from CO₂⁺ UVD emissions.

Overall, the shapes of the average profiles from each period are similar, with temperatures nearly constant or gradually increasing with height, especially within the 150-180 km altitude range. The profiles from the first two sampling periods in particular show a gradual increase in temperature with height until roughly 180-190 km, where more isothermal structure is seen. The later sampling periods all show roughly isothermal temperatures throughout most of the profile.

Isothermal temperatures have been used to characterize the upper dayside thermosphere structure in conjunction with the variable location of the traditional exobase (~170 to 185 km) [e.g. *Vaille et al.*, 2010; *Vaille et al.*, 2009]. In reality, the exobase is not a fixed al-

altitude that separates collisional (thermosphere) and collisionless (exosphere) regimes, but rather a transition region over which collisions gradually diminish in importance with increasing altitude [Vaille *et al.*, 2010; Bougher *et al.*, 2015c]. Modern atomic O exosphere models confirm that this transitional domain extends from ~ 135 km up to approximately 300 km on the Mars dayside. Therefore, the hydrostatic assumption also reasonably holds throughout this transitional region (i.e. specifically above the traditional exobase and approaching ~ 300 km). Also, it has been found through global model simulations that the altitude level where isothermal temperatures begin varies with solar activity, increasing in altitude as the solar cycle approaches solar maximum conditions [Bougher *et al.*, 1999, 2015b]. Since this is a function of thermospheric heating, seasonal changes may also contribute to the varying altitude level of isothermal temperatures. Between these two groups of profiles (spanning orbits 1086 to 1900) notable seasonal changes as well as decreasing solar activity might be contributing to this decreasing altitude of the onset of isothermal temperatures (see later discussion in this section).

The horizontal bars along the profiles in Figure 2 show the standard deviation of the temperature at several altitude levels over the sample period. This illustrates the orbit-to-orbit intrinsic variability in the upper atmosphere. Averaged over all orbit periods and the 150-180 km altitude range, the magnitude of this variability is ± 24 K for both CO₂ and Ar derived temperatures. Within this altitude range, orbits 865-885 show the least variability with an average standard deviation of ± 15.5 K while the greatest variability is observed during orbits 2023-2150 with an average standard deviation of ± 30.9 K.

Table 4 shows the average values of the temperatures and scale heights derived from the NGIMS Ar and CO₂ densities for each sampling period. These values were calculated

by taking the average of each of the profiles in Figure 2 over the 150-180 km altitude range. The average CO₂ derived temperatures are plotted over time and solar longitude in Figure 3. The first period of orbits, from Ls = 306-308, has the warmest temperature of any of the sampling periods, at 242.0 ± 15.5 K. The following sampling period shows temperatures cooling as equinox approaches (Ls = 0). This trend continues past equinox, with a consistent decrease in temperature over time. During Ls = 69-75, a low temperature of 174.7 ± 24.2 is reached, producing a near 70 K difference in temperature between this and the first NGIMS sampling period. By the next sampling period at Ls = 126-135, the temperature has increased by about 20 K. However, the final sampling period shows the lowest average temperature of any of the orbit periods, at 168.3 ± 21.8 K.

Recall that the seasonal cycle (including the effects of changing heliocentric distance) and solar cycle both contribute to changes in thermospheric temperatures over longer time scales. The EUV-UV flux, which is an important source of heating in the thermosphere, varies as a function of both the heliocentric distance and solar activity (see section 1). Included in Figure 4 is a plot of the daily mean Lyman-alpha UV irradiance measured by the MAVEN EUV Monitor (EUVM). The effects of changing heliocentric distance are visible in the large scale sinusoidal trend in the Lyman-alpha irradiance, with a minimum value observed near aphelion (Ls = 71) and a maximum value observed near perihelion (Ls = 251). The higher frequency wave corresponds to the 27-day solar rotation. This EUVM instrument has a unique capability to quantify the actual EUV irradiance at Mars, with potentially important differences with respect to solar fluxes provided by Earth based solar flux models (rotated to Mars). Discrepancies between Earth measurement derived estimates and EUVM measurements of Lyman-alpha at Mars have a standard deviation

of 3.4% over the period considered in this study and exceed 10% during periods of high solar activity. This important topic is the subject of a future paper.

The sampling periods for NGIMS and the average solar longitude and Mars-Sun distance for each period are presented in Figure 5. The first NGIMS orbit period during Ls = 306-308 is the closest of any of the periods to perihelion. The relatively small heliocentric distance should result in a greater solar EUV-UV flux reaching Mars (assuming all else, including solar activity, is fairly constant) and thus increased thermospheric heating and warmer temperatures. A relatively high Lyman-alpha irradiance is observed for this sampling period as seen in Figure 4, as well as the warmest average temperature of the NGIMS analysis.

Throughout the next three orbit periods, heliocentric distance increases and the season changes from southern hemisphere summer to autumn as the equinox passes ($L_s = 0$). The decrease in EUV-UV flux reaching Mars is evident in the trend in Lyman-alpha irradiance in Figure 4, which has a reduction in magnitude by nearly a half from near perihelion to the approach of aphelion. When the effects of heliocentric distance were removed from the Lyman-alpha irradiance, an overall decreasing trend was still present, characterized by a reduction in magnitude by $\sim 15\%$ from the first sampling period to the fourth. Thus, though the increase in heliocentric distance seems to be the strongest driver of the decrease in Lyman-alpha irradiance during this time, gradually decreasing solar activity is also a contributing factor, though to a lesser extent. The steady decrease of temperatures over the same time period mirrors this decrease in Lyman-alpha irradiance, indicating the decreasing EUV-UV flux (largely as a function of increasing heliocentric distance and

to a lesser degree decreasing solar activity) strongly contributed to this thermospheric temperature trend.

The sampling period during $L_s = 69-75$ includes aphelion at $L_s = 71$, the farthest Mars-Sun distance. A relatively low average temperature of 174.7 ± 24.2 K was extracted for this period. At the same time, the effect of the large heliocentric distance can be seen in the low magnitude Lyman-alpha irradiance. With less EUV-UV radiation contributing to heating in the thermosphere, temperatures would be expected to be relatively low. Thus, the low average thermospheric temperature observed during $L_s = 69-75$ is likely in great part due to the peak in heliocentric distance.

After aphelion, heliocentric distance begins to decrease again. In Figure 4, a corresponding $\sim 20\%$ increase in Lyman-alpha irradiance is observed between aphelion and $L_s \sim 160$. Additionally, during the last two sampling periods, MAVEN began observing the northern hemisphere summer. The increase in temperature by about 20 K during the $L_s = 126-135$ sampling period thus likely corresponds to a combination of these factors.

Temperatures reach their lowest value in the last NGIMS sampling period. This orbit period is during $L_s = 153-156$, approaching northern hemisphere autumnal equinox, with heliocentric distance decreasing and Lyman-alpha irradiance still increasing. If heliocentric distance, season, and solar activity were the only drivers of temperature in the thermosphere, temperatures would be expected to continue rising. Additional processes are thus likely driving the observed decrease in temperatures. As the thermosphere can also be strongly coupled to the lower atmosphere [*Bougher et al.*, 2015a], effects from below could also be driving this temperature change. Another factor that may contribute is the diurnal cycle. While most other sampling periods were observed at a local time of

noon to late afternoon, the period spanning $L_s = 153-156$ was the earliest in the morning, as can be seen in Table 2. Several modeling studies have found significant day-night temperature contrast in the thermosphere [Bougher *et al.*, 2015b; González-Galindo *et al.*, 2009]. Close to equinox for solar minimum conditions (the closest approximate conditions to the $L_s = 153-156$ sampling period), the diurnal temperature range has been estimated to be ~ 90 K [Bougher *et al.*, 2015b]. However, at this point, there is too limited local time coverage in the dataset to confirm the role of the diurnal cycle in this trend.

Overall, the phase of the trend in dayside thermospheric temperatures closely agrees with that in the Lyman-alpha irradiances. Using Lyman-alpha irradiance as a proxy for the EUV-UV flux, which is made variable by changing solar activity and heliocentric distance, temperatures appear to be responding strongly to solar forcing during this time period.

Additionally, for each of the sampling periods, the density at a constant altitude can be examined for this same trend with respect to Lyman-alpha irradiances. Specifically, looking at densities from NGIMS at the lowest altitude sampled in all the periods (159 km) gives some insight into trends at the lower end of our altitude range as well as coupling with the atmospheric column below. This is shown in Figure 6, which includes both Ar and CO₂ densities at 159 km for each sampling period. The pattern of averaged densities at an altitude of 159 km clearly reveals the same general trend seen in the average temperatures over 150-180 km. This implies that at about 160 km, average densities also vary primarily due to changing heliocentric distance. However, this effect is likely a combination of the atmospheric seasonal response near 160 km as well as the seasonal response of the atmospheric column below. Multiple altitudes at/below 160 km would need to be sampled

in order to extract the separate roles of the lower and upper atmosphere in controlling density variations at 160 km.

4.2. NGIMS and IUVS scale height trends and comparisons

The average scale heights extracted from each IUVS sampling period are included in Table 3. These scale heights derived from IUVS measured dayglow emission can be compared with scale heights calculated from the NGIMS CO₂ derived temperatures. This comparison is seen in Figure 7, which shows average scale heights for both NGIMS, in black, and IUVS, in red, as a function of date and solar longitude. It is apparent that the IUVS scale height trend is consistent with the trend seen in the NGIMS data, especially within the range of the 1-sigma orbit-to-orbit variability for each.

As can be seen in Figure 5, the IUVS analysis does have a sampling period earlier than could be used for NGIMS during Ls = 217-219, before perihelion. During this time period near the Comet Siding Spring encounter, the largest IUVS scale heights are observed, at 13.4 ± 1.3 km. The next IUVS sampling period, from Ls = 306-310, partially overlaps with the NGIMS period from Ls = 306-308. At this time, the NGIMS average scale height was 13.6 ± 0.9 km while the IUVS average scale height was 13.3 ± 0.7 km. These values are very close in magnitude. Like NGIMS, IUVS scale heights decrease after Ls = 306-310. A minimum scale height is observed for IUVS at Ls = 54-65, at 10.0 ± 1.0 km. This period also overlaps with an NGIMS sampling period. The NGIMS sampling period at Ls = 54-65 has an average scale height of 10.5 ± 1.7 km, within one standard deviation of the IUVS value. From near perihelion to near aphelion, IUVS average scale heights show a 3.3 km decrease in scale height while NGIMS shows a 3.1 km decrease in scale height over about the same time. Furthermore, the last sampling period from

IUVS at $L_s = 133-147$ shows a scale height value of 10.7 ± 0.7 km. This increase in average scale heights agrees with the increase in scale height values observed by NGIMS during this time period. Overall, there is strong agreement seen in the scale height trends observed by NGIMS and IUVS as well as agreement in the magnitude of the average scale heights themselves at the points where the sampling periods overlap in time. Relatively small differences in scale height during these periods of overlapping observations are likely attributable to the differences in viewing geometry between IUVS and NGIMS.

Additional comparisons were made by examining the correlation between the trends in EUV-UV flux and heliocentric distance and average scale height. Variation of scale height with Lyman-alpha irradiance and heliocentric distance is shown in Figure 8. Since there was good agreement between the NGIMS and IUVS averaged scale heights, all the sampling periods from NGIMS and IUVS were combined into one dataset. Scale height was then compared to Lyman-alpha irradiance measured by EUVM on MAVEN. The resulting linear Pearson correlation coefficient was 0.88, showing a high correlation between Lyman-alpha irradiance and scale height trends over this time period. This would indicate that solar forcing is a strong driver of upper thermospheric temperatures for the solar conditions during this portion of the MAVEN mission. (Note that the MAVEN mission thus far has coincided with solar moderate to minimum conditions.) Furthermore, when comparing the scale height trend to the heliocentric distance, a correlation coefficient of -0.84 is produced. This high anticorrelation with heliocentric distance indicates that the variability in EUV-UV flux received at Mars due to the Mars-Sun distance plays a significant role in driving the variability in thermospheric temperatures, more so than other intrinsic solar variability on this time scale. Notably, the farthest outlying point

seen in Figure 8 corresponds to the last NGIMS sampling period which was observed at the earliest local time with a low temperature of 168.3 ± 21.8 K. If this NGIMS sampling period is removed from the analysis, then the correlation between scale height and Lyman-alpha irradiance and the anticorrelation between scale height and heliocentric distance become somewhat stronger, with correlation coefficients of 0.94 and -0.95, respectively. This may further indicate that during the last sampling period, EUV-UV flux is not as significant a driver of thermospheric temperatures as at other times, and other processes might have a stronger influence. In addition to Lyman-alpha irradiances, the trend in scale heights was compared to 17-22 nm irradiances, also measured by EUVM on MAVEN. A slightly lower (though still strong) correlation is seen in this EUV band with a correlation coefficient of 0.83 using the combined NGIMS and IUVS dataset. It is possible that this correlation is slightly lower due to the more strident solar rotation signature in the 17-22 nm irradiances than in the Lyman-alpha irradiances.

4.3. Comparison of M-GITM predicted temperatures and NGIMS temperatures

Two sampling periods are chosen for comparison of M-GITM simulated temperatures and NGIMS derived temperatures: $L_s = 327-330$ (orbits 1059-1086) and $L_s = 69-75$ (orbits 2194-2274). The former corresponds to near vernal equinox (solar moderate) conditions. The latter is associated closely with aphelion (solar minimum) conditions. M-GITM archived datasets are selected that most closely match these vernal equinox (VEQUMED) and aphelion (APHMIN) sampling conditions. Recall that the M-GITM code (developed prior to MAVEN) is primarily solar driven and is thus far designed to capture the major processes that regulate the thermospheric energetics and dynamics on longer time scales [Bougher *et al.*, 2015b].

Simulated temperatures are extracted from M-GITM along the NGIMS provided spacecraft trajectory (below 250 km) for each orbit contained in these two sampling periods. Inbound orbit legs are solely used at this point, yielding a suite of temperature profiles for each sampling period that are subsequently averaged together. Finally, the averaged temperature profiles are used to further extract 150-180 km temperatures, for computing a final altitude averaged temperature. These M-GITM temperature values of ~ 236 K (VEQUMED) and ~ 172 K (APHMIN) are superimposed on the temperature trend illustrated in Figure 3.

It is notable that the M-GITM absolute temperatures (above) and the combined seasonal/solar activity trend simulated over these two sampling periods ($\Delta T \sim 64$ K) is very similar to that derived from NGIMS temperatures ($\Delta T \sim 54$ K) (see Table 4). This suggests that the dayside thermal budget simulated in the M-GITM code captures the combined solar forcing (EUV-UV heating) and cooling processes (CO_2 15- μm cooling and molecular thermal conduction) needed to reasonably reproduce dayside temperature variations over 150-180 km. In addition, wave forcing effects may not be important in maintaining low SZA temperatures in the Martian thermosphere, similar to that found in other model simulations [Medvedev *et al.*, 2015]. Further confirmation requires a detailed comparison of model and measured NGIMS O and CO_2 densities as a function of altitude for constraining CO_2 cooling rates within the MGITM model (see Bougher *et al.* [2015a]). This task is beyond the scope of this paper.

4.4. Current MAVEN results contrasted with previous dayglow observations

The temperatures and scale heights obtained in the present study can be directly contrasted with the values from previous studies over the same altitude region (150-180 km)

with relatively low SZAs. Specifically, the *Jain et al.* [2015] dayglow analysis revealed a temperature change from 300 K to 250 K (corresponding to a scale height change from 16.2 to 14.0), between $L_s = 218$ and $L_s = 337-352$. This 50 K decrease in temperature from a time before perihelion to near northern hemisphere spring equinox was attributed to changing solar forcing. This seasonal range has been extended in the present study, with a ~ 70 K decrease in temperature from before perihelion to aphelion. Slight differences in scale heights ($\sim 10\%$) derived from IUVS observations between this study and *Jain et al.* [2015] are largely attributable to the current use of a Chapman fit, as seen in Figure 1, on the CO_2^+ UVD emission intensity rather than an exponential fit [*Jain*, 2016]. Significantly, in both analyses, solar forcing was identified as the main driver of the long-term change in thermospheric temperatures and scale heights over this altitude range.

It is also important that the *Jain et al.* [2015] study found that on shorter time scales (e.g. from 5-16 May 2015), temperatures showed no correlation with the EUV flux, as indicated by the 17-22 nm irradiance measured by EUVM. A similar short-term study was conducted seeking a correlation of dayside temperatures (from NGIMS sampling) and EUV-UV fluxes over 24 days (spanning orbits 2023-2150) to examine the role of solar forcing on a shorter time scale. Both the daily median 17-22 nm irradiances and daily mean Lyman-alpha irradiances were used. No correlation was found between the EUV-UV flux and temperatures over this shorter time scale of about 24 days, with correlation coefficients of 0.07 (Lyman-alpha) and 0.10 (17-22 nm). Thus, in agreement with *Jain et al.* [2015], it can be concluded that over longer time scales (over at least several months), dayside temperature variability in the Martian thermosphere is driven primarily by solar

forcing. Over shorter time scales, however, temperatures do not seem to respond to solar forcing, possibly due to the much smaller change in the net solar flux arriving at Mars or the stronger influence of waves [e.g. *Stiepen et al.*, 2015].

Interestingly, the *Stiepen et al.* [2015] analysis of temperatures and scale heights derived from Mars Express SPICAM dayglow observations (over the same altitude region with relatively low SZAs) came to different conclusions. In this study, ten years worth of upper atmospheric scale heights were compared to the EUV flux (as indicated by the Mars-rotated F10.7-cm index), but no correlation was identified (see section 1.1). This was interpreted to mean that variability in solar flux received at the top of the Martian atmosphere was not the dominant driver of variability in thermospheric scale heights over this time period. Two possible factors which may contribute to this discrepancy in the conclusions of these two studies are: (a) differences in data sampling frequency and data analysis techniques, specifically in the averaging of the datasets, and (b) differences in solar proxies used to characterize the solar EUV-UV forcing (yielding thermospheric heating) at Mars. In the study presented here, designated short-term sampling period scale heights and temperatures were averaged and subsequently the long-term trend of those sampling period averages were examined. This technique was applied because of the large intrinsic variability of the upper atmosphere on a day-to-day time scale. This approach is different from that employed in the *Stiepen et al.* [2015] study, which used a 10-year period of derived scale heights but did not average any of these in smaller time scale sampling periods. It is likely that the averaging performed in the analysis presented in this paper served to smooth some of this orbit-to-orbit variability, permitting the underlying solar forcing component to be observed. The implication of this is that orbit-to-orbit variations

in scale height (caused by various potential sources such as solar flares or gravity waves) appear to dominate over solar EUV driven seasonal variability in scale height on these short timescales in the thermosphere. Furthermore, MAVEN IUVS (12-scans for each of 5-orbits per day) and NGIMS (5-orbits per day) sampling is of much higher frequency than the available Mars Express SPICAM dayglow limb scans. This means that temporal sampling is more sparse for SPICAM measurements. Finally, a solar EUV proxy measured at Mars is inherently better than the F10.7-cm index measured at Earth and corrected for the Sun-Earth-Mars angle (i.e. the latter cannot account for the changing face of the Sun and the corresponding temporal variations in the solar EUV fluxes received at Earth and Mars).

5. Conclusions and future work

Mars dayside upper atmosphere temperature trends driven by seasonal and solar activity are clearly revealed by measurements from the MAVEN mission from October 2014 to May 2016. NGIMS observations show a trend in Mars dayside thermospheric temperatures that largely responds to the changing solar fluxes received at the planet. During the period of NGIMS observations, solar forcing is primarily regulated by the changing season (from near perihelion to after aphelion). Average temperatures derived from CO₂ densities decrease after perihelion from 242.0 ± 15.5 K to 174.7 ± 24.2 K at aphelion, a difference of ~ 70 K. The strong correlation between scale height and Mars-Sun distance demonstrates the highly significant effects of changing heliocentric distance on thermospheric scale heights at this time. Since it is difficult to completely separate solar declination driven latitudinal effects (pure seasonal effects) from the effects of changing heliocentric distance, solar declination effects likely contributed to some of the variability

along the overarching scale height trend. Furthermore, a decline in solar activity at the same time may also contribute to this solar forcing trend, though to a lesser extent than the changing heliocentric distance.

Average scale heights were also derived from the MAVEN IUVS dayglow observations, using the CO_2^+ UVD emission intensity. The IUVS and NGIMS datasets were then compared over the same altitude range, 150 - 180 km, for $\text{SZA} \leq 75^\circ$. NGIMS and IUVS dayside thermosphere scale height trends are found to strongly agree, especially within one standard deviation (the 1-sigma intrinsic orbit-to-orbit variability). Both show maximum scale heights near perihelion, decreasing scale heights until aphelion, and a slight increase in scale height somewhat thereafter. Furthermore, on occasions when sampling periods overlap in time, scale heights from both instruments were similar, and remained within the 1-sigma range of both. In short, this study reconciles in-situ (NGIMS) and remote (IUVS) dayglow measurements for the first time, yielding a consistent characterization of the dayside thermosphere scale height and temperature trends.

These combined observations from both NGIMS and IUVS indicate that during this time period within the MAVEN mission (spanning solar moderate to minimum conditions), the Mars dayside thermospheric temperature variability on longer time scales (at least several months) is largely tied to solar driven thermal balances. Using Lyman-alpha irradiance measured by the EUV monitor on MAVEN as an indicator of EUV-UV heating, a trend is observed with decreasing irradiance from near perihelion to right before aphelion. Since the primary source of heating in the thermosphere comes from EUV heating, (see reviews by *Bougher et al.* [1999, 2015a]), this trend would indicate increased EUV heating near perihelion and decreased heating near aphelion. Correspondingly, the warmest average

temperature (and highest scale height) is observed near perihelion and a low average temperature (and scale height) near aphelion. Though variability in EUV-UV irradiance is due to both the seasonal cycle (including the changing heliocentric distance) and solar activity, and both may contribute to especially the first half of the observed trend, variation in heliocentric distance appears to be the most significant factor contributing to temperature and scale height trends during these observations. The last NGIMS sampling period, however, does not seem to follow this trend in EUV-UV flux, demonstrating that other processes may still (at times) have a significant effect on thermospheric temperatures. Furthermore, the influence of solar forcing was not seen over shorter time scales (~ 24 days). Overall, there is strong evidence that solar forcing over long time scales is largely driving thermospheric temperature trends during the MAVEN mission thus far. These conclusions differ from those in *Stiepen et al.* [2015] (as well as *Leblanc et al.* [2006]) which found thermospheric temperatures derived from SPICAM dayglow observations not to be driven by solar forcing over longer time scales. However, differences in the frequency of data sampling, averaging techniques, and the solar proxy used could be contributing to the difference in conclusions.

Three-dimensional model simulations from M-GITM have also yielded thermosphere temperatures (150-180 km) along the orbit trajectories for comparison to those derived from NGIMS densities. Two sampling periods were chosen, corresponding to near vernal equinox (solar moderate) to aphelion (solar minimum) conditions. Simulated temperatures ranged from 236 K to 172 K, in contrast to NGIMS averaged values of 228 K to 175 K. The fact that the solar driven M-GITM model is able to reasonably reproduce this NGIMS derived temperature variation is further confirmation of solar forcing serving as

the primary driver of dayside temperature variations over long time scales. These lower SZA temperature trends (under solar control) may not be the same as those at higher SZA (i.e. high latitude, near the terminator and onto the nightside). Numerical studies capturing gravity wave processes (i.e. both momentum and energy depositions) suggest that gravity waves effects may indeed be important at high latitudes and onto the nightside [e.g. *Medvedev et al.*, 2015]. Further data-model comparisons are needed at higher SZA to quantify the importance of these non-solar processes.

Measurements characterizing upper atmosphere temperatures during both extremes of the Martian seasons and the solar cycle have not yet been completed. The period of MAVEN observations used in this analysis covers near perihelion to near autumnal equinox, with solar cycle conditions changing from solar moderate to solar minimum.

This yielded observations at aphelion for solar minimum conditions (the lower extreme of temperatures resulting from combined solar cycle and seasonal variability) with a temperature of 174.7 ± 24.2 K. This value is similar to temperatures observed by previous spacecraft and simulated by M-GITM for similar conditions. However, the next Martian aphelion should be even deeper into solar minimum conditions, such that further observations at this time could find somewhat lower temperatures. Furthermore, during perihelion near solar maximum conditions (the other extreme), dayside temperatures should be much warmer than seen in NGIMS observations near perihelion for solar moderate conditions (242.0 ± 15.5 K). However, as solar maximum should not occur for several more years, the MAVEN mission may not be able to provide this characterization of the upper atmosphere.

In order to expand this research, continued low SZA dayside measurements are needed by multiple instruments to confirm and further extend the longer term (solar driven) and shorter term (wave driven) trends in dayside temperatures first identified in *Jain et al.* [2015]. This includes both MAVEN IUVS and NGIMS measurements resulting in derived temperatures, as well as EUVM measurements of solar Lyman-alpha and EUV fluxes. Furthermore, different IUVS techniques for extraction of temperatures from dayglow limb profiles should continue to be explored. Finally, detailed numerical model calculations of energy deposition by solar EUV fluxes and gravity waves must be compared to determine the relative roles of each in maintaining dayside temperatures and driving their day-to-day variability. Pilot studies for gravity wave heating/cooling are being conducted and appear promising [*England et al.*, 2016].

Acknowledgments. Funding support for this research was provided by the MAVEN project. Also, A. Stiepen was supported by the Fund for Scientific Research (F.R.S.-FNRS). All NGIMS, IUVS, and EUVM datasets used in this paper are available on the public version of the MAVEN Science Data Center (SDC) website at LASP (<https://lasp.colorado.edu/maven/sdc/public/>) as well as the Planetary Data System (PDS). Likewise, all datacubes containing the M-GITM model temperatures used for comparison with NGIMS derived values in this paper are taken from the model archive also found on the MAVEN public website.

References

- Bougher, S. W., S. Engel, R. G. Roble, and B. Foster (1999), Comparative terrestrial planet thermospheres 2. Solar cycle variation of global structure and winds at equinox, *J. Geophys. Res.*, *104*, 16,591–16,611, doi:10.1029/1998JE001019.
- Bougher, S. W., S. Engel, R. G. Roble, and B. Foster (2000), Comparative terrestrial planet thermospheres 3. Solar cycle variation of global structure and winds at solstices, *J. Geophys. Res.*, *105*, 17,669–17,692, doi:10.1029/1999JE001232.
- Bougher, S. W., R. G. Roble, and T. Fuller-Rowell (2002), Simulations of the upper atmospheres of the terrestrial planets, *Geophysical Monograph Series*, *130*, 261–288.
- Bougher, S. W., J. M. Bell, J. R. Murphy, M. A. Lopez-Valverde, and P. G. Withers (2006), Polar warming in the Mars thermosphere: Seasonal variations owing to changing insolation and dust distributions, *Geophys. Res. Lett.*, *33*, L02,203, doi:10.1029/2005GL024059.
- Bougher, S. W., T. E. Cravens, J. Grebowksy, and J. Luhmann (2015a), The aeronomy

of Mars: Characterization by MAVEN of the upper atmosphere reservoir that regulates volatile escape, *Space Sci. Reviews*, *195*, 423–456, doi:doi:10.1007/s11214-014-0053-7.

Bougher, S. W., D. Pawlowski, J. M. Bell, S. Nelli, T. McDunn, J. R. Murphy, M. Chizek, and A. Ridley (2015b), Mars global ionosphere-thermosphere model: Solar cycle, seasonal, and diurnal variations of the Mars upper atmosphere, *J. Geophys. Res.*, *120*, 311–342, doi:doi:10.1002/2014JE004715.

Bougher, S. W., B. M. Jakosky, J. Halekas, J. Grebowsky, J. G. Luhmann, and others (2015c), Early MAVEN dip deep campaign reveals thermosphere and ionosphere variability, *Science*, *350*, 1–7, doi:doi:10.1126/science.aad0459.

Bougher, S. W., J. M. Bell, K. Olsen, K. Roeten, P. R. Mahaffy, M. Elrod, M. Benna, and B. M. Jakosky (2015d), Variability of Mars thermospheric neutral structure from MAVEN deep dip observations: NGIMS comparisons with global models, *EOS*, *2015 Supplement*(74805).

Cui, J., R. V. Yelle, V. Vuitton, J. H. Waite Jr, W. T. Kasprzak, D. A. Gell, H. B. Niemann, I. C. F. Muller-Wodarg, N. Borggren, G. G. Fletcher, E. L. Patrick, E. Raaen, and B. A. Magee (2009), Analysis of Titan's neutral upper atmosphere from Cassini Ion Neutral Mass Spectrometer measurements, *Icarus*, *200*, 581–615.

England, S. L., G. Liu, E. Yigit, P. R. Mahaffy, M. Elrod, M. Benna, H. Nakagawa, N. Terada, and B. M. Jakosky (2016), MAVEN NGIMS observations of atmospheric gravity waves in the Martian thermosphere, *J. Geophys. Res.*, *this issue*.

Eparvier, F., P. C. Chamberlin, T. N. Woods, and E. B. M. Thiemann (2015), The Solar Extreme Ultraviolet Monitor for MAVEN, *Space Sci. Reviews*, *195*, 293–301, doi:doi:10.1007/s11214-015-0195-2.

Forbes, J. M., F. G. Lemoine, S. L. Bruinsma, M. D. Smith, and X. Zhang (2008), Solar flux variability of mars' exosphere densities and temperatures, *Geophysical Research Letters*, *35*(1).

Fox, J. L., and K. Y. Sung (2001), Solar activity variations of the Venus thermosphere/ionosphere, *J. Geophys. Res.*, *106*, 21,305–21,336, doi:10.1029/2001JA000069.

González-Galindo, F., F. Forget, M. López-Valverde, M. Angelats i Coll, and E. Millour (2009), A ground-to-exosphere martian general circulation model: 1. seasonal, diurnal, and solar cycle variation of thermospheric temperatures, *Journal of Geophysical Research: Planets*, *114*(E4).

Haberle, R. M., J. L. Hollingsworth, A. Colaprete, A. F. C. Bridger, C. P. McKay, J. R. Murphy, J. Schaeffer, , and R. Freedman (2003), The NASA/AMES Mars General Circulation Model: Model Improvements and comparison with observations, in *Published Conference Abstract, International Workshop: Mars Atmosphere Modelling and Observations*.

Huestis, D. L., T. G. Slanger, B. D. Sharpee, and J. L. Fox (2010), Chemical origins of the mars ultraviolet dayglow, *Faraday Discussions*, *147*, 307–322.

Jain, S. K., A. I. F. Stewart, N. M. Schneider, J. Deighan, A. Stiepen, J. S. Evans, M. H. Stevens, M. S. Chaffin, M. Crismani, W. E. McClintock, J. T. Clarke, G. M. Holsclaw, D. Y. Lo, F. Fefevre, F. Montmessin, E. M. B. Thiemann, F. Eparvier, and B. M. Jakosky (2015), The structure and variability of Mars upper atmosphere as seen in MAVEN/IUVS dayglow observations, *Geophys. Res. Lett.*, *42*, 9023–9030, doi:10.1002/2015GL065419.

Jain, S. K. e. a. (2016), Response of Martian dayglow to solar EUV and XUV flux, *J. Geophys. Res., this issue.*

Jakosky, B. M., R. P. Lin, J. M. Grebowksy, J. G. Luhmann, and others (2015), The Mars Atmosphere and Volatile Evolution (MAVEN) Mission, *Space Sci. Reviews*, 195, 3–48, doi:doi:10.1007/s11214-015-0139-x.

Keating, G. M., S. W. Bougher, R. W. Zurek, R. H. Tolson, G. J. Cancro, S. N. Noll, J. S. Parker, T. J. Schellenberg, R. W. Shane, B. L. Wilkerson, J. R. Murphy, J. L. Hollingsworth, R. M. Haberle, M. Joshi, J. C. Pearl, B. J. Conrath, M. D. Smith, R. T. Clancy, R. C. Blanchard, R. G. Wilmoth, D. F. Rault, T. Z. Martin, D. T. Lyons, P. B. Esposito, M. D. Johnston, C. W. Whetzel, C. G. Justus, and J. M. Babicke (1998), The Structure of the Upper Atmosphere of Mars: In Situ Accelerometer Measurements from Mars Global Surveyor, *Science*, 279, 1672–1676, doi:10.1126/science.279.5357.1672.

Keating, G. M., M. E. Theriot, R. H. Tolson, S. W. Bougher, F. Forget, M. A. i Coll, and J. M. Forbes (2003), Recent detection of winter polar warming in the Mars upper atmosphere, in *The Third International Mars Polar Science Conference*, p. 8033, pasadena, California.

Keating, G. M., S. W. Bougher, M. E. Theriot, and R. H. Tolson (2008), Properties of the Mars Upper Atmosphere Derived from Accelerometer Measurements, in *Proceedings of the 37th COSPAR Scientific Assembly*, montreal, Canada.

Leblanc, F., J. Y. Chaufray, J. Lilensten, O. Witasse, and J.-L. Bertaux (2006), Martian dayglow as seen by the SPICAM UV spectrograph on Mars Express, *Journal of Geophysical Research*, 111(E09S11), doi:10.1029/2005JE002664.

- Lo, D. Y., R. V. Yelle, N. M. Schneider, S. K. Jain, A. I. F. Stewart, S. L. England, J. I. Deighan, A. Stiepen, J. S. Evans, M. H. Stevens, M. S. Chaffin, M. M. J. Crismani, W. E. McClintock, J. T. Clarke, G. M. Holsclaw, F. Lefvre, and B. M. Jakosky (2015), Nonmigrating tides in the martian atmosphere as observed by maven iuvs, *Geophysical Research Letters*, *42*(21), 9057–9063, doi:10.1002/2015GL066268.
- López-Valverde, M. A., D. P. Edwards, M. López-Puertas, and C. Roldán (1998), Non-local thermodynamic equilibrium in general circulation models of the Martian atmosphere 1. Effects of the local thermodynamic equilibrium approximation on thermal cooling and solar heating, *J. Geophys. Res.*, *1031*, 16,799–16,812, doi:10.1029/98JE01601.
- Mahaffy, P. R., M. Benna, M. Elrod, R. V. Yelle, S. W. Bougher, S. W. Stone, and B. M. Jakosky (2015a), Structure and composition of the neutral upper atmosphere of Mars from the MAVEN NGIMS investigation, *Geophys. Res. Lett.*, *42*, 8951–8957, doi:10.1002/2015GL065329.
- Mahaffy, P. R., M. Benna, T. King, D. N. Harpold, and R. e. a. Arvey (2015b), The Neutral Gas and Ion Mass Spectrometer on the Mars Atmosphere and Volatile Evolution Mission, *Space Sci. Reviews*, *195*, 49–73, doi:doi:10.1007/s11214-014-0091-1.
- McClintock, W. E., N. M. Schneider, G. M. Holsclaw, J. T. Clarke, A. C. Hoskins, I. Stewart, F. Montmessin, R. V. Yelle, and J. Deighan (2014), The Imaging Ultraviolet Spectrograph (IUVS) for the MAVEN Mission, *Space Science Reviews*, *195*(1), 75–124, doi:10.1007/s11214-014-0098-7.
- Medvedev, A., and E. Yigit (2012), Thermal effects of internal gravity waves in the Martian upper atmosphere, *Geophys. Res. Lett.*, *39*, doi:10.1029/2012GL050852.

Medvedev, A., E. Yigit, P. Hartough, and E. Becker (2011), Influence of gravity waves on the Martian atmosphere: General circulation modeling, *J. Geophys. Res.*, *116*, doi:10.1029/2011JE003848.

Medvedev, A., E. Yigit, T. Kuroda, and P. Hartough (2013), General circulation modeling of the Martian upper atmosphere during global dust storms, *J. Geophys. Res.*, *118*, 2234–2246, doi:10.1002/2013JE004429.

Medvedev, A., F. Gonzalez-Galindo, E. Yigit, A. G. Feofilov, F. Forget, and P. Hartough (2015), Cooling of the Martian thermosphere by CO₂ radiation and gravity waves: An intercomparison study with two general circulation models, *J. Geophys. Res.*, *120*, 913–927, doi:10.1002/2015JE004802.

Mendillo, M., C. Narvaez, G. Lawler, W. Kofman, J. Mouginot, D. Morgan, and D. Gurnett (2015), The equivalent slab thickness of Mars' ionosphere: Implications for thermospheric temperatures, *Geophys. Res. Lett.*, *42*, 3560–3568, doi:10.1002/2015GL063096.

Mueller-Wodarg, I. C. F., D. F. Strobel, J. I. Moses, J. H. Waite, J. Crovisier, R. V. Yelle, S. W. Bougher, and R.-G. Roble (2008), Neutral Atmospheres, *Space Sci. Rev.*, *139*, 191–234, doi:10.1007/s11214-008-9404-6.

Nier, A., and M. B. McElroy (1977), Composition and structure of mars' upper atmosphere: Results from the neutral mass spectrometers on viking 1 and 2, *Journal of Geophysical Research*, *82*(28), 4341–4349.

Ridley, A., Y. Deng, and G. Tòth (2006), The global ionosphere-thermosphere model, *J. Atmos. Sol-Terr. Phys.*, *68*, 839.

Seiff, A., and D. B. Kirk (1977), Structure of the atmosphere of mars in summer at mid-latitudes, *Journal of Geophysical Research*, *82*(28), 4364–4378.

- Snowden, D., R.-V. Yelle, J. Cui, J.-E. Wahlund, N. J. T. Edberg, and K. Agren (2013), The thermal structure of Titan's upper atmosphere: 1. Temperature profiles from Cassini INMS observations, *Icarus*, *226*, 552–582, doi:10.1016/j.icarus.2013.06.006.
- Stewart, A. I. (1972), Mariner 6 and 7 ultraviolet spectrometer experiment: Implications for CO_2^+ , CO and O airglow, *Journal of Geophysical Research*, *77*, 1.
- Stewart, A. I., C. Barth, C. Hord, and A. Lane (1972), Mariner 9 ultraviolet spectrometer experiment: Structure of Mars' upper atmosphere, *Icarus*, *17*(2), 469–474.
- Stewart, A. I. F. (1987), Revised time dependent model of the Martian atmosphere for use in orbit lifetime and sustenance studies, in *LASP-JPL Internal Report, NQ-802429*, Jet Propulsion Laboratory.
- Stiepen, A., J.-C. Gerard, S. W. Bougher, F. Montmessin, and B. Hubert (2015), Mars thermospheric scale heights from CO Cameron and CO_2^+ dayglow observations from Mars Express, *Icarus*, *245*, 295–305, doi:10.1016/j.icarus.2014.09.051.
- Teolis, B. D., M. E. Perry, B. A. Magee, J. Westlake, and J. H. Waite (2010), Detection and measurement of ice grains and gas distribution in the Enceladus plume by Cassini's Ion Neutral Mass Spectrometer, *J. Geophys. Res.*, *115*, doi:doi:10.1029/2009JA015192.
- Vaille, A., M. R. Combi, S. W. Bougher, V. Tishchev, , and A. F. Nagy (2009), Three-dimensional study of Mars upper thermosphere-ionosphere and hot oxygen corona: 2. Solar cycle, seasonal variations, and evolution over history, *J. Geophys. Res.*, *114*(E11006), doi:10.1029/2009JE003389.
- Vaille, A., M. R. Combi, V. Tishchev, S. W. Bougher, and A. F. Nagy (2010), A study of suprathermal oxygen atoms in Mars upper thermosphere and exosphere over the range of limiting conditions, *Icarus*, *206*(1), 18–27.

Woods, T., and G. Rottman (2002), Solar ultraviolet variability over time periods of aeronomic interest, *Atmospheres in the Solar System: Comparative Aeronomy, Geophys. Monogr. Ser.*, 130, 221.

Zurek, R. W., R. H. Tolson, D. Baird, M. Z. Johnson, and S. W. Bougher (2015), Application of MAVEN accelerometer and attitude control data to Mars atmospheric characterization, *Space Sci. Reviews*, 195, 303–317, doi:doi:10.1007/s11214-014-0095-x.

Accepted Article

Table 1. Pre-MAVEN Spacecraft Observations of the Mars Upper Atmosphere ^a

Mission	Dates	F10.7 ^b	Ls (deg)	D _{S-M} ^c (AU)	SZA (deg)	Temperature (K)
Mariner 4	15 July 1965	77	139	1.55	67	212
Viking 1 Lander	20 July 1976	69	96	1.65	44	186
Viking 2 Lander	3 Sept. 1976	76	117	1.61	44	145
Mars Global Surveyor 1 ^d	16 Jan. 1998	93	256	1.38	74	220
Mars Global Surveyor 2 ^e	27 Oct. 1998	127	49	1.65	57	230
Mars Express ^f	Oct.-Dec. 2004	105	100-138	1.63	15-37	197

^a Table is adapted from Table 1 in *Bougher et al.* [2000]

^b F10.7 index (in units of 10^{-22} W/m²/Hz) measured at Earth

^c Mars-Sun distance

^d Mars Global Surveyor phase 1 aerobraking sample

^e Mars Global Surveyor phase 2 aerobraking sample

^f SPICAM dayglow observations [*Leblanc et al.*, 2006]

Table 2. Characteristics of NGIMS sampling periods

Orbits	N ^a	Dates	Ls (deg)	Z _p ^b (km)	SZA ^c (deg)	Lat ^c (deg)	LT ^c (hr)
865 - 885	19	3/11/15 - 3/15/15	306 - 308	158	54 - 69	10 - 24	15.0 - 15.6
1059 - 1086	28	4/17/15 - 4/22/15	327 - 330	150	1 - 13	-22 - -11	11.4 - 12.0
1900 - 2000	89	9/20/15 - 10/9/15	44 - 53	153	50 - 73	-51 - -30	11.8 - 13.9
2023 - 2150	115	10/14/15 - 11/7/15	54 - 65	156	47 - 59	-39 - -10	9.3 - 11.7
2194 - 2274	77	11/15/15 - 11/30/15	69 - 75	150	57 - 72	-11 - 8	7.2 - 8.7
2873 - 2974	88	3/22/16 - 4/10/16	126-135	159	49 - 74	66 - 74	11.9 - 18.7
3165 - 3192	24	5/15/16 - 5/20/16	153 - 156	157	63 - 72	38 - 52	7.0 - 8.0

^a Number of orbits

^b Minimum altitude for sampling period

^c Minimum and maximum values of solar zenith angle, latitude, and local time, respectively

Table 3. Characteristics of IUVS sampling periods.

Orbits	N ^a	Dates	Ls (deg)	D _{S-M} ^b (AU)	SZA ^c (deg)	Lat ^c (deg)	LT ^c (hr)	H ^d (km)
109 - 128	19	10/18/14 - 10/22/14	218	1.40	32 - 72	34 - 53	9 - 14	13.4 ± 1.3
866 - 896	22	03/11/15 - 03/17/15	308	1.44	52 - 75	4 - -19	15 - 18	13.3 ± 0.7
973 - 988	14	04/01/15 - 04/03/15	318	1.46	26 - 74	-33 - 33	14 - 16	12.9 ± 1.0
1051	1	04/15/15 - 04/15/15	320	1.48	33 - 60	25 - -34	13 - 14	13.0 ± 0.6
1160 - 1309	43	05/05/15 - 06/02/15	345	1.52	12 - 73	17 - -75	8 - 12	11.6 ± 1.0
2023 - 2150	93	10/14/15 - 11/07/15	61	1.66	49 - 75	11 - -47	7 - 11	10.0 ± 1.0
2951 - 3099	114	04/05/16 - 05/03/16	140	1.56	15 - 75	15 - 70	9 - 18	10.7 ± 0.7

^a Number of orbits

^b Mars-Sun distance

^c Minimum and maximum values of solar zenith angle, latitude, and local time, respectively

^d Scale height

Table 4. Temperatures (T) and scale heights (H) derived from NGIMS Ar and CO₂ densities

Orbits	T _{CO₂} (K)	H _{CO₂} (km)	T _{Ar} (K)	H _{Ar} (km)
865 - 885	242.0 ± 15.5	13.6 ± 0.9	245.1 ± 15.6	15.1 ± 1.0
1059 - 1086	228.3 ± 24.3	12.8 ± 1.4	228.1 ± 23.2	14.1 ± 1.4
1900 - 2000	200.2 ± 27.5	11.2 ± 1.5	205.6 ± 27.7	12.7 ± 1.7
2023 - 2150	187.0 ± 30.9	10.5 ± 1.7	194.3 ± 31.6	12.0 ± 2.0
2194 - 2274	174.7 ± 24.2	9.8 ± 1.4	182.4 ± 24.1	11.2 ± 1.5
2873 - 2974	194.2 ± 21.5	10.9 ± 1.2	199.9 ± 21.5	12.4 ± 1.3
3165 - 3192	168.3 ± 21.8	9.4 ± 1.2	173.6 ± 21.6	10.7 ± 1.3

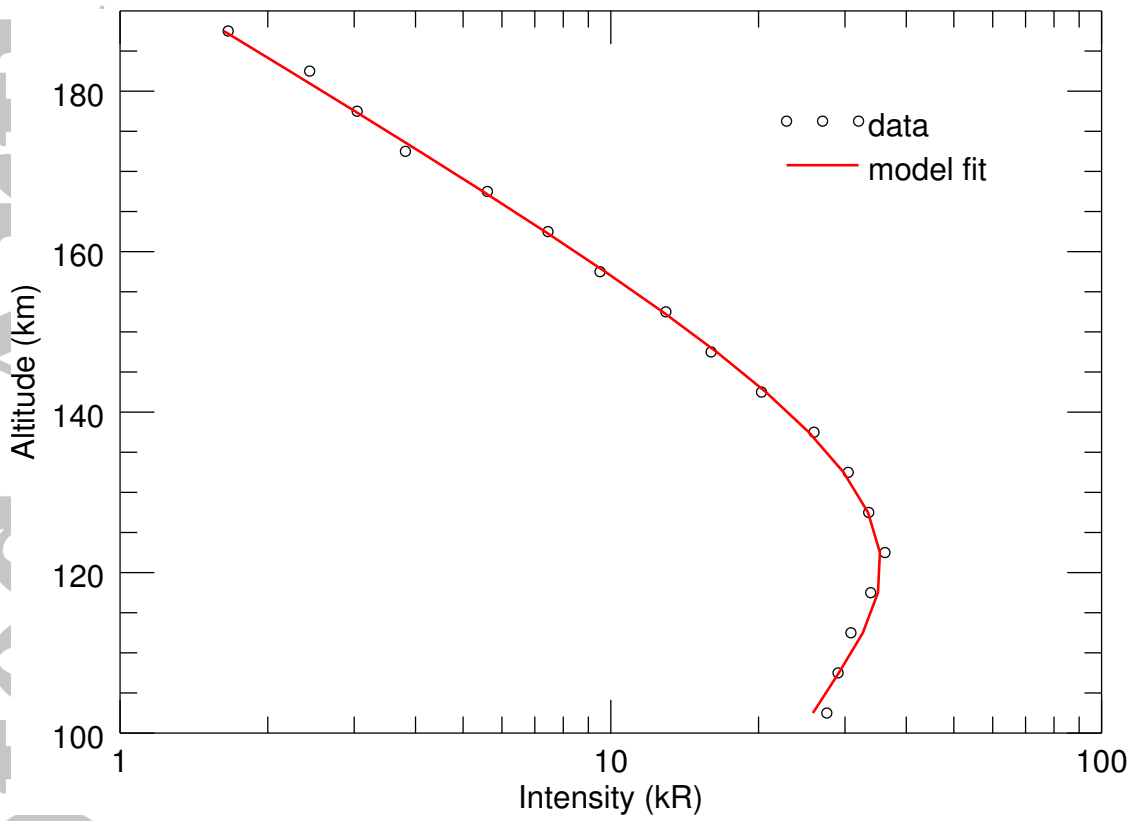


Figure 1. Solid symbols show the intensity of CO_2^+ from scan two of orbit 110 (10 Oct. 2014). The red curve shows the empirical Chapman fit.

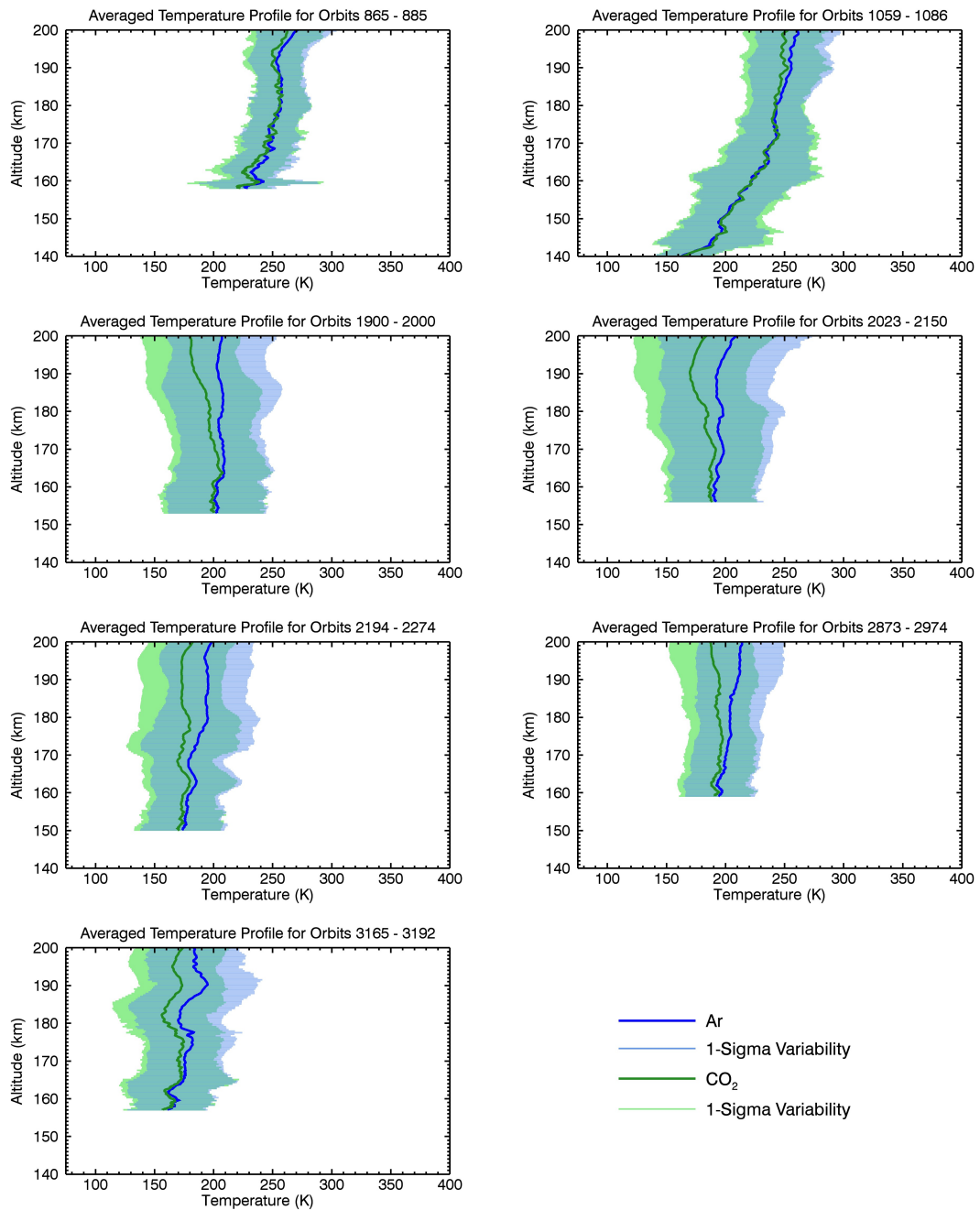


Figure 2. Averaged Ar (blue) and CO₂ (green) derived temperature profiles for each NGIMS sampling period. The horizontal bars show the standard deviation (due to intrinsic variability) along the profile. Note that the altitude range here is slightly larger than the 150-180 km range used in the analysis.

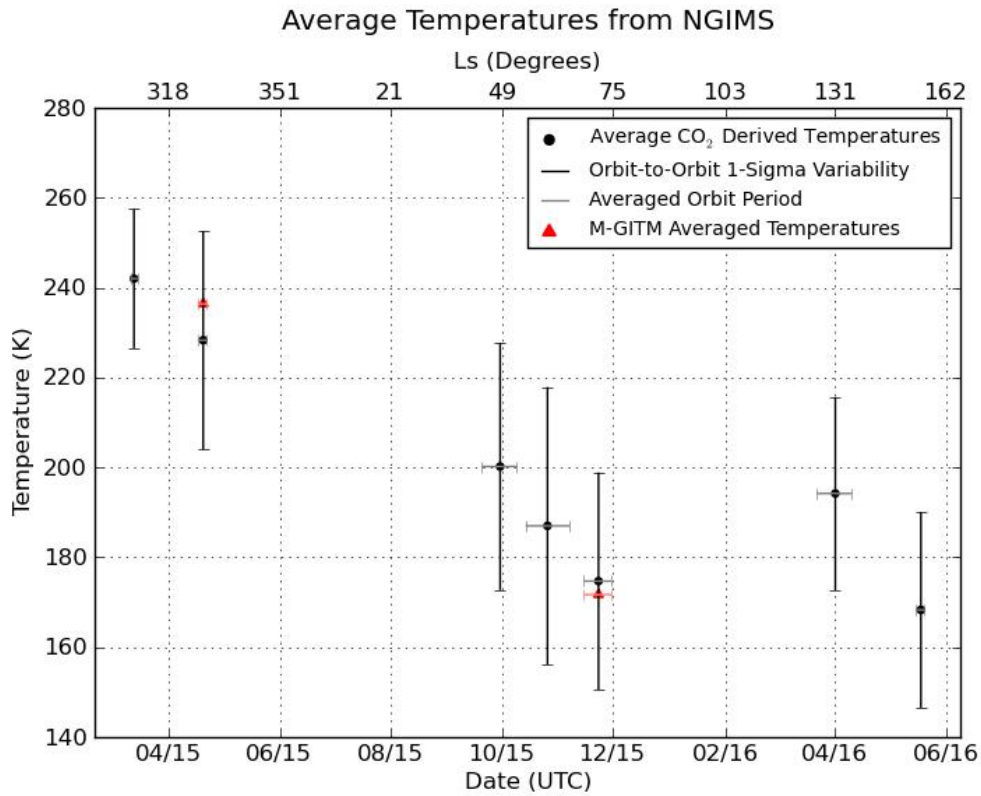


Figure 3. Average temperatures over 150-180 km for each NGIMS sample period. Vertical bars show the orbit-to-orbit standard deviation in temperature and horizontal bars show the time over which the average was taken for each period. Red triangles show M-GITM average temperatures for certain sampling periods.

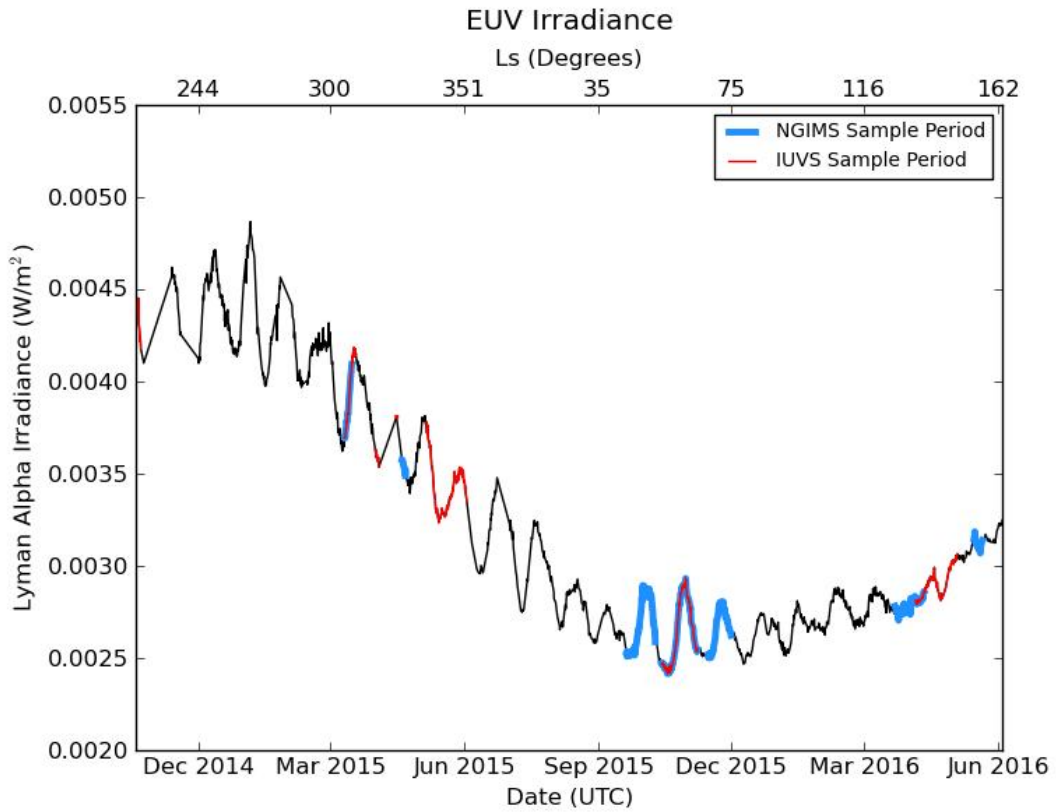


Figure 4. Time series of the daily mean Lyman-alpha irradiance measured by the EUV monitor on MAVEN from 19 October 2014 to 3 June 2016. The blue line segments show the time of the NGIMS sampling periods and the red line segments show the time of the IUVS sampling periods.

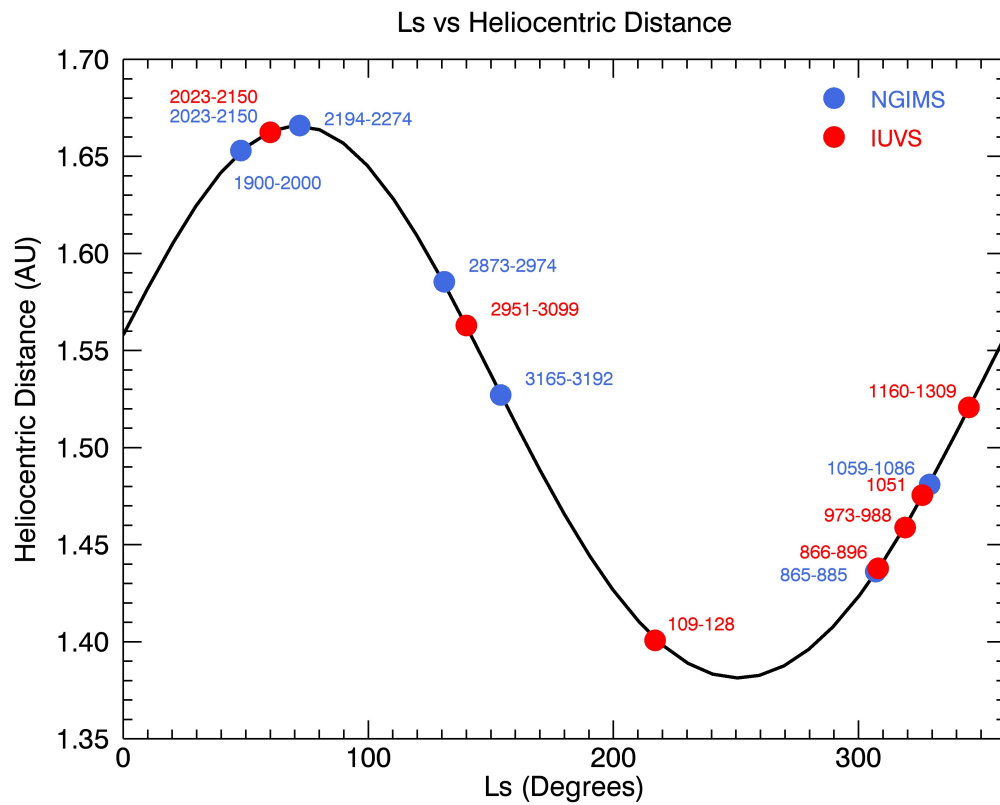


Figure 5. The black curve shows the relation between the solar longitude (Ls) and heliocentric distance for Mars. The circles on this curve show the average heliocentric distance and Ls for each sampling period for both NGIMS (blue) and IUVS (red).

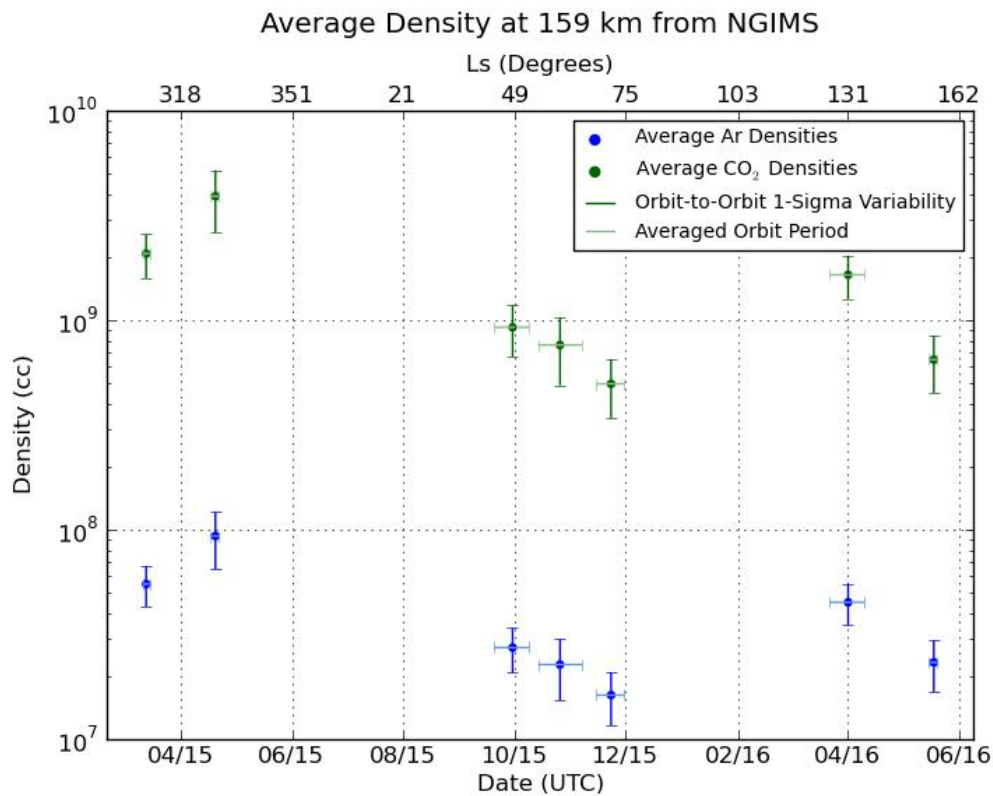


Figure 6. The densities (number per cubic centimeter) for Argon (blue) and CO₂ (green) at 159 km (the lowest altitude sampled in all periods) averaged over each sampling period. Vertical bars show the orbit-to-orbit standard deviation in density and horizontal bars show the time over which each average was taken.

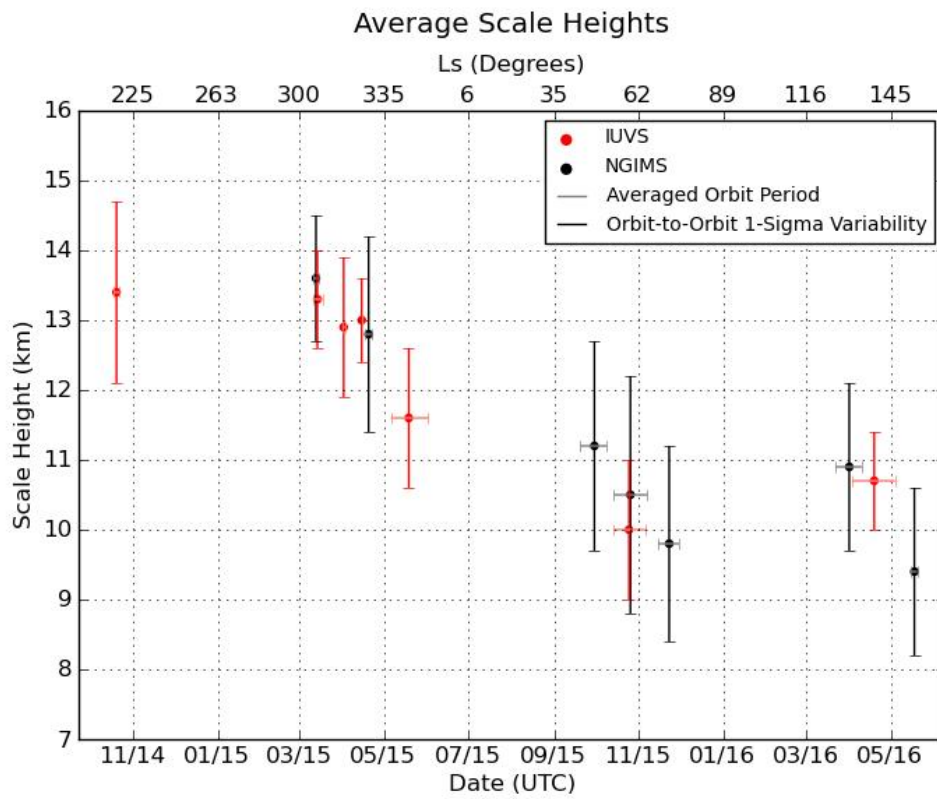


Figure 7. Average scale heights over 150-180 km for each sample period from both NGIMS (black) and IUVS (red). Vertical bars show the orbit-to-orbit standard deviation in scale heights and horizontal bars show the time over which the average was taken for each period.

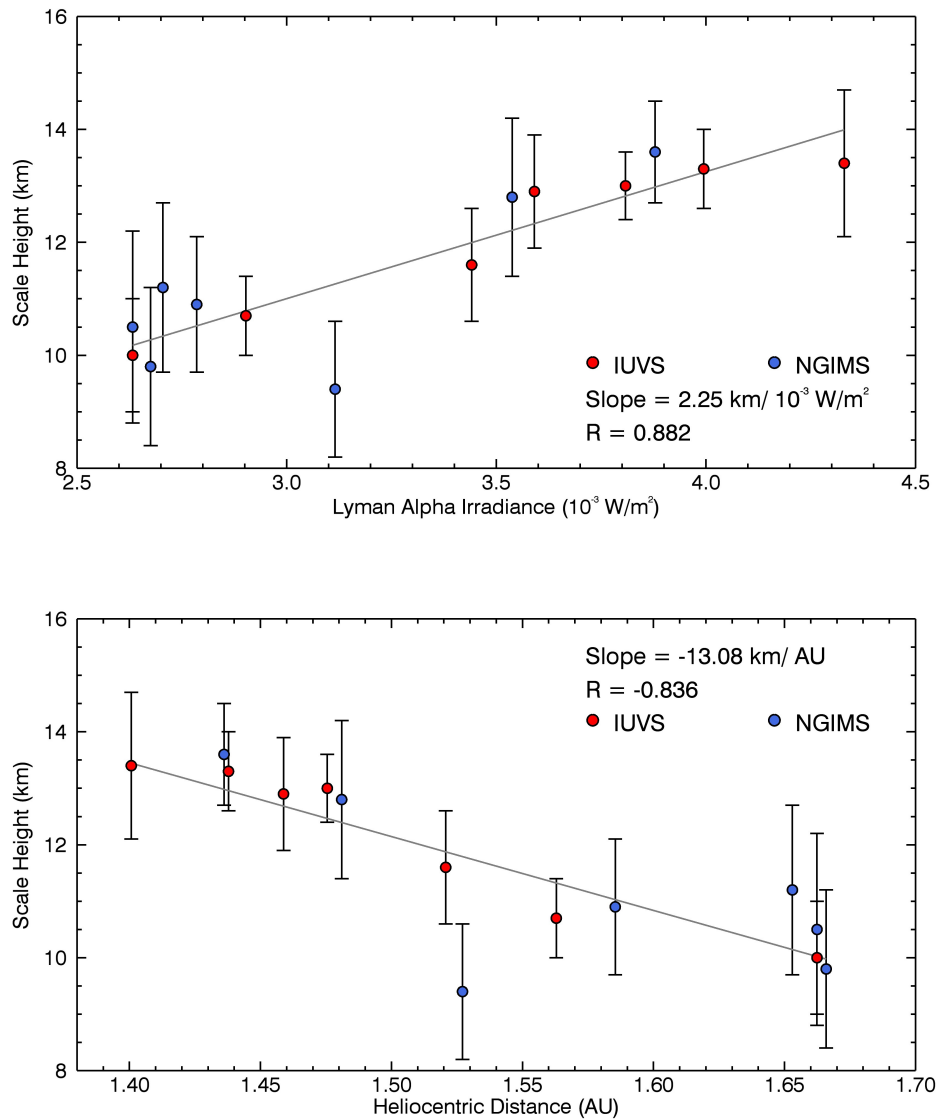


Figure 8. Variation of scale height with Lyman-alpha irradiance measured by the EUV monitor on MAVEN (top) and scale height with heliocentric distance (bottom). Both IUVS and NGIMS sampling periods were combined for this analysis. The line of best fit and slope from a linear regression is included as well as the linear Pearson correlation coefficient, R .